



One-pot hydrothermal fabrication of layered β -Ni(OH)₂/g-C₃N₄ nanohybrids for enhanced photocatalytic water splitting

Junqing Yan^{a,**}, Huan Wu^a, Hong Chen^a, Liuqing Pang^a, Yunxia Zhang^a, Ruibin Jiang^a, Landong Li^c, Shengzhong (Frank) Liu^{a,b,*}

^a Shaanxi Engineering Lab for Advanced Energy Technology, School of Materials Science and Engineering, Shaanxi Normal University, Xi'an 710119, PR China

^b State key Laboratory of Catalysis, iChEM, Dalian Institute of Chemical Physics, Dalian National Laboratory for Clean Energy, Chinese Academy of Sciences, Dalian 116023, PR China

^c School of Material Science and Engineering & National Institute for Advanced Materials, Nankai University, Tianjin 30071, PR China

ARTICLE INFO

Article history:

Received 20 March 2016

Received in revised form 22 April 2016

Accepted 24 April 2016

Available online 27 April 2016

Keywords:

β -Ni(OH)₂/g-C₃N₄

Nanohybrids

Hydrothermal

Water photo-splitting

Nanolayers

ABSTRACT

Exfoliation and assembly of 2-D materials have been extensively investigated to exploit their performances in the area of catalysis, magnetics and electronics etc., but novel strategies are highly desired to shorten their preparing period and to improve their environment-friendliness. Here we introduce a simple and green hydrothermal process to fabricate ultrathin layered β -Ni(OH)₂/g-C₃N₄ nanohybrids for photocatalytic water splitting application. Different from conventionally separated exfoliation and assembly, the exfoliation of g-C₃N₄, formation of β -Ni(OH)₂ as well as their self-assembly can be one-pot achieved by simple hydrothermal treatment of nickel dichloride and bulk g-C₃N₄ free of any organic agents for 12 h. Moreover, the thickness of β -Ni(OH)₂ nanolayer can be adjusted by controlling the concentration of nickel precursors. The as-obtained nanohybrids have been in detail characterized to have a strong interaction of the assembly components, among which the g-C₃N₄ is active for photocatalytic water splitting, and β -Ni(OH)₂ nanolayer is efficient for acceleration of activation of water oxidation. Their photocatalytic water splitting performances are evaluated in the presence of sacrificial agents, based on which the assembly of β -Ni(OH)₂ nanolayers on the surface of exfoliated g-C₃N₄ lamella is found to obviously promote the charge separation, water oxidation kinetics as well as final photocatalytic performances compared to the pristine g-C₃N₄. The direct water splitting is also achieved with the AQY of 1.48% under 405-nm visible light irradiation. The one-pot hydrothermal method introduced here may be an alternative strategy for g-C₃N₄, a promising photocatalytic water splitting material, to construct highly efficient solar energy conversion composite systems based on its exfoliated lamella.

© 2016 Elsevier B.V. All rights reserved.

1. Introduction

Two-dimensional (2-D) layered materials, owing to the distinctive and exceptional properties such as ultrahigh electron mobility, large surface area, more adsorption and reactive sites, have attracted extensive attention for potential application in the areas of environment remediation, energy conversion and storage in recent years [1–3]. The discovery of graphene, a typical 2-D material, has triggered the great interest in preparing 2-D nanosheets [4–6], especially for the 2-D metal-free covalent organic polymer

nanosheets. For example, a class of metal-free graphitic polymers consisting of unique honeycomb network such as carbon nitrides (C₃N₄) [2–6], boron carbon nitride [7] and boron carbide [8] have been developed and employed for synthesis of monolayer of carbon atoms. C₃N₄ has been successfully prepared with several allotropes and the graphitic phase generally known as g-C₃N₄ has been proved to be the stable property under ambient conditions [2–6,9–14]. Bulk g-C₃N₄ is a typical graphite-like layered material, which weak van der Waals force ensures layer-by-layer structure and tri-s-triazine units connecting with planar amino groups forming each layer (Fig. S1) [9,10]. Pristine g-C₃N₄ can be easily obtained via one-step simple thermal condensation of nitrogen-rich precursors, such as urea, cyanamide and dicyandiamide etc. [10].

In order to improve its specific surface area, reactive sites as well as photocatalytic performances, exfoliation of the 2-D g-C₃N₄ material has been thus investigated by massive processes, such

* Corresponding author at: Shaanxi Engineering Lab for Advanced Energy Technology, School of Materials Science and Engineering, Shaanxi Normal University, Xi'an 710119, PR China.

** Corresponding author.

E-mail addresses: junqingyan@snnu.edu.cn (J. Yan), liusz@snnu.edu.cn (S. Liu).

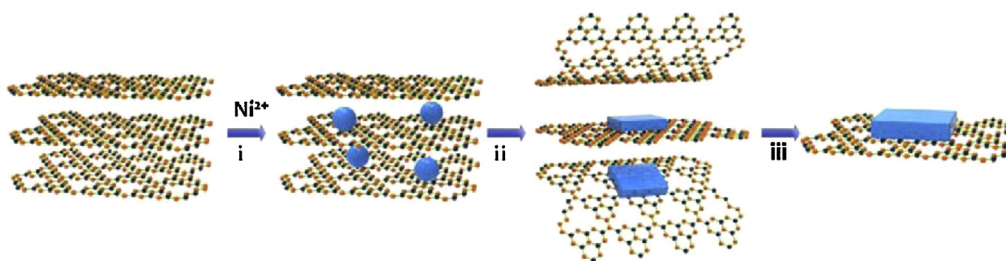


Fig. 1. Schematic illustration of β -Ni(OH) $_2$ nanosheet's formation with the assistance of the bulk g-C $_3$ N $_4$ for the construction of lamellar nanohybrids. (i) Ni $^{2+}$ ions insert into the layered g-C $_3$ N $_4$ framework at the initial stage; (ii) the adsorbed Ni $^{2+}$ ions achieve the process of heterogeneous nucleation between the g-C $_3$ N $_4$ layers, which restrict β -Ni(OH) $_2$ nanosheet's formation with exposed (001) facets at the intermediate stage; (iii) at the final stage, the layered Ni(OH) $_2$ /C $_3$ N $_4$ nanohybrids formed after the self-exfoliation of g-C $_3$ N $_4$.

as sonication-assisted liquid-exfoliation method with organic solvent [5] or concentrated inorganic acid [11]. However, it should be pointed out that the mentioned conventional exfoliation of g-C $_3$ N $_4$ usually undergoes a long preparing period of over one week, contains unfavorable non-environmental-friendly organic solvent and exhibits a relatively low yield of product. Moreover, the exfoliation of the nanolayers as well as fabrication of composites or hybrids based on them is necessarily separated. Another usage of the exfoliated mono or multiple nanolayers is to introduce foreign component for fabricating composites such as face-to-face layered hybrid nanojunctions [14], for promotion of performances benefitted from distinctive coordinated effect. For example, Hou et al., constructed MoS $_2$ /g-C $_3$ N $_4$ thin layered heterojunctions by impregnating at the first step and subsequently via sulfidation process, the obtained hybrid layered nanojunctions gave an excellent photocatalytic hydrogen generation [14]. Meanwhile, the polymeric tri-s-triazine network contains some N-docking sites, which have been proved to be the adsorption sites of foreign species. Based on this thought, Zhang et al., loaded Co $_3$ O $_4$ nanoparticles with size of 3 nm on the surface of g-C $_3$ N $_4$ to enhance photocatalytic water oxidation activity [13]. To date, it is still challenging to simultaneously succeed exfoliation and assembly of composite in one-pot, and development of a fast and green exfoliation route is also desirable.

Recently, direct water splitting through the wireless powder photocatalytic system has been proved to represent the promising technology for the conversion of solar energy to chemical fuel from water [15]. Like other semiconductors, g-C $_3$ N $_4$ also suffers from the unavoidable and undesired problems of photogenerated charge recombination and migration, and some suitable redox cocatalysts have been employed with the detectable photocatalytic activity [16–22]. The main roles of the cocatalysts focus on accelerating the migration of carriers and enhancing the water splitting reaction kinetics. It should be mentioned that the former derives from the Fermi energy difference of the semiconductor and cocatalyst, and the latter is the cocatalyst electrochemical properties [23,24]. An appropriate cocatalyst should be a better electrolyst with the excellent electrolytic water performance [25].

β -Ni(OH) $_2$ is an efficient electrochemical material owing to its high energy density and good electrochemical stability in alkaline electrolyte [25,26], which has been widely applied for impressive water splitting reactions and specially the oxygen evolution reaction (OER) [27–29]. The β -Ni(OH) $_2$ nanosheet can be easily obtained under specific systems [25,27,29]. The distinctive feature of Ni(OH) $_2$ is that it can be *in situ* oxidized to NiOOH, which lowers the Fermi energy of Ni(OH) $_2$ electrocatalyst and then increases the Fermi energy difference between semiconductor and electrocatalyst [30]. Also, the NiOOH species can bring about a better Helmholtz layer potential drop at the electrocatalyst/electrolyte junction, which promotes the OER kinetics [23].

However, Ni(OH) $_2$ electrocatalyst is rare reported to be applied in the wireless powder photocatalytic reaction, especially the special structure system [31]. Herein, to solve the carrier separation and achieve a better water splitting performance of g-C $_3$ N $_4$, we introduce a novel one-pot hydrothermal process to construct layered β -Ni(OH) $_2$ /C $_3$ N $_4$ nanohybrid using bulk g-C $_3$ N $_4$ and nickel dichloride (NiCl $_2$) as precursors. The bulk g-C $_3$ N $_4$ powder was exfoliated into single layers, into which Ni $^{2+}$ cations were inserted and induced to form β -Ni(OH) $_2$ nanosheets, causing *in situ* construction of layered Ni(OH) $_2$ /C $_3$ N $_4$ nanohybrids. The β -Ni(OH) $_2$ nanosheets was found to act as the receiver of photogenerated holes, and then this process achieves the effective separation of carriers.

2. Experimental section

All of the chemical reagents of analytical grade were purchased from Alfa Aesar Chemical Co., and used as received without further purification.

Synthesis of Ni(OH) $_2$ /C $_3$ N $_4$ lamellar nanohybrids: Bulk g-C $_3$ N $_4$ was first synthesized via the thermal condensation of urea under the nitrogen atmosphere at 550 °C for 4 h, and the obtained yellow sample was then grinded into ultrafine powders for further use. Typically, 0.5 g grinded bulk g-C $_3$ N $_4$ and a calculated NiCl $_2$ were mixed into 60 mL deionized water. The blue mixture was stirred for ca. 30 min at room temperature and then transferred to 80 mL Teflon stainless steel autoclave, which was sealed and maintained at 120 °C for 12 h in an air dry oven. When the autoclave was naturally cooled to room temperature, the resulting powder was collected and washed with distilled water and ethanol three times. The obtained light blue powder was dried at 80 °C for 12 h. The as-fabricated samples are denoted as xwt% Ni(OH) $_2$ /C $_3$ N $_4$, where “x” stands for the weight content of Ni(OH) $_2$.

2.1. Synthesis of reference samples

As for discussion, the exfoliation of g-C $_3$ N $_4$ was also examined in 0.01 M HCl media but free of nickel ions by following the above hydrothermal route. The as-obtained sample is denoted as C $_3$ N $_4$ -HCl. Similarly, the hydrothermal treatment of pure 0.1 g NiCl $_2$ free of g-C $_3$ N $_4$ and mineralizer was also carried out. It was confirmed by XRD patterns that a single phase of Ni(OH) $_2$ will be formed in this case. To illustrate the superiority of above synthesized Ni(OH) $_2$ /C $_3$ N $_4$ nanohybrids, 0.5% Ni(OH) $_2$ /C $_3$ N $_4$ compound was also synthesized via a simple impregnation method employing the synthesized layered g-C $_3$ N $_4$ and Ni(OH) $_2$.

2.2. Characterization techniques

The X-ray diffraction (XRD) patterns of the studied samples were recorded on a Rigaku Smartlab – 9 kW powder diffractometer by

using Cu K α X-ray ($\lambda = 1.54186 \text{ \AA}$) tubes at a scanning rate of $4^\circ/\text{min}$ in the region of $2\theta = 10\text{--}80^\circ$.

Raman analysis was carried out on a Renishaw InVia Raman spectrometer and the spectra were obtained with the green line of an Ar-ion laser (514.53 nm) in micro-Raman configuration.

Diffuse reflectance UV–vis near-infrared (UV–vis-NIR) spectra of studied samples (ca. 20 mg diluted in ca. 80 mg BaSO₄) were recorded in the air against BaSO₄ in the region of 200–1000 nm on a PerkinElmer Lambda 950 spectrophotometer.

Transmission electron microscopy (TEM) images were taken on a FEI Tecnai G2 F20 electron microscope at an acceleration voltage of 200 kV. A few drops of alcohol suspension containing the sample were placed on a carbon-coated copper grid, followed by evaporation at ambient temperature.

X-ray photoelectron spectra (XPS) were recorded on a Kratos Axis Ultra DLD spectrometer with a monochromated Al-K α X-ray source ($h\nu = 1486.6 \text{ eV}$), hybrid (magnetic/electrostatic) optics and a multi-channel plate and delay line detector (DLD). All spectra were recorded by using an aperture slot of $300 \times 700 \mu\text{m}$, and survey spectra were recorded with a pass energy of 160 eV and high-resolution spectra with a pass energy of 40 eV. Accurate binding energies ($\pm 0.1 \text{ eV}$) were determined with respect to the position of the adventitious C 1s peak at 284.8 eV.

Fourier transform infrared reflectance (FTIR) spectra of samples were carried out on a Bruker EQUINX55 spectrometer with 128 scans at a resolution of 2 cm^{-1} . The spectra were recorded in dry air with KBr as the background.

Photoluminescence (PL) spectra were recorded on a PerkinElmer LS55 fluorescence spectrophotometer. The samples of ca. 200 mg were dry-pressed into self-supporting wafers and then illuminated by an incident light of 320 nm at ambient temperature.

2.3. Electrocatalytic measurement

Elemental analysis was conducted in a conventional three-electrode cell on a Zennium Zahner electrochemical workstation with the Ag/AgCl (saturated KCl) and Pt as the reference and counter electrode, respectively. The studied samples were ground roughly and then 5 mg was dispersed in 0.5 mL of DMF. The mixture was sonicated to obtain a slurry, which was spread onto FTO glass (NOTE: FTO glass should be treated through sonication in acetone, ethanol and deionized water, successively, and then nitrogen purging to ensure catalysts coating successfully). To improve adhesion, the working electrode was further dried at 373 K for 2 h. The electrolyte was 0.1 M NaOH and the scan rate were 50 mV/s for OER and HER measurements. Photocurrent response was carried out on the same electrochemical workstation with 0.5 M Na₂SO₄ as the electrolyte (pH 6.8).

2.4. Photocatalytic water splitting tests

Photocatalytic water splitting performances were evaluated in a home-made side-irradiation-type Pyrex reaction cell connected to a closed gas circulation and evacuation system under the irradiation of 150 W Xe lamp with the wavelength ranging from 200 to 2500 nm. In a typical experiment, catalyst sample of 200 mg was suspended in ca. 200 mL aqueous solution, containing 0.01 M AgNO₃ for O₂ generation and 10% (v/v) triethanolamine-water solution for H₂ generation. After being evacuated for 30 min, the reactor cell was irradiated at a constant temperature of 298 K under stirring. The overall water splitting was carried out using the pure water. The gaseous products were analyzed by an on-line gas chromatograph (Shanghai GC122) with a thermal conductivity detector.

3. Results and discussion

3.1. Synthesis and characterizations of $\beta\text{-Ni(OH)}_2/\text{g-C}_3\text{N}_4$ hybrids

Fig. 1 gives a schematic illustration on the exfoliation of g-C₃N₄ as well as its induced *in situ* formation and assembly of $\beta\text{-Ni(OH)}_2$ nanosheet. At the initial stage, the divalent nickel ions with ionic radius of ca. 0.07 nm are inserted into the layered C₃N₄ material. Subsequently, the inserted Ni²⁺ cations are proposed to undergo slow heterogeneous nucleation, restricted growth and finally come into being crystalline $\beta\text{-Ni(OH)}_2$ nanosheets under the hindering effect of layers of g-C₃N₄ carrier, and this process oppositely promotes the self-exfoliation of bulk g-C₃N₄, causing *in situ* self-assembly and fabrication of $\beta\text{-Ni(OH)}_2/\text{g-C}_3\text{N}_4$ hybrids. Similar simultaneous induction, exfoliation and self-assembly processes have been observed for fabrication of layered graphene and $\beta\text{-Ni(OH)}_2$ hybrids [32]. To confirm the above-mentioned exfoliation and self-assembly, several typical samples were first prepared, which include: (i) pure bulk g-C₃N₄; (ii) hydrothermal treated g-C₃N₄ in the environment of hydrochloric acid but free of Ni²⁺ cations (denoted as C₃N₄-HCl); (iii) hydrothermal treated g-C₃N₄ with different content of Ni²⁺ ions added free of hydrochloric acid (denoted as “x” wt% Ni(OH)₂/C₃N₄, where x stands for the content of nickel ions). The detailed synthesis procedures are given in the Section 2.

To obtain the direct information about microstructure of studied g-C₃N₄ series compounds, transmission electron microscopy (TEM) was carried out and the typical images are shown in Fig. 2. Clearly, the bulk g-C₃N₄ sample exhibits the typical dark and non-transparent massive structure with smooth external surface [9,13]. However, as for the C₃N₄-HCl sample achieved by hydrothermal treatment using low concentration of hydrochloric acid as the solvent, multilayered g-C₃N₄ nanosheets with thickness of ca. 5 nm appear in the TEM visual field (Fig. 2b), which demonstrates that it is feasible to achieve the exfoliation of g-C₃N₄ by the hydrothermal method. Fig. 2c–f show the representative TEM images of Ni(OH)₂/C₃N₄ samples as a function of nickel contents, which were synthesized via hydrothermal treatment of mixture of nickel dichloride and bulk g-C₃N₄ without hydrochloric acid added. Similarly, transparent multilayer g-C₃N₄ nanosheets can be observed for all these samples, but those surfaces that are covered with distinguished extent of Ni(OH)₂ platelets will be characterized and confirmed later. With increased amount of the addition of nickel ions, the Ni(OH)₂ nanosheets tend to be layer-by-layer aggregated on the surface of multilayer C₃N₄ nanosheet based on the extent of darkness. It should be pointed out that the increased amount of Ni(OH)₂ nanosheets does not obviously cause the overlap of the exfoliated C₃N₄ nanosheets, which proves that the exfoliation of C₃N₄ just happens during the nucleation, growth, formation and self-assembly of the Ni(OH)₂.

To detect the structure and phase information about our synthesized samples, X-ray diffraction (XRD) technology was carried out. As given in Fig. 3, only one diffraction peak at 27.3° ($d = 0.326 \text{ nm}$) originating from the (002) interlayer diffraction of the graphitic-like C₃N₄ structure can be found for the C₃N₄-HCl sample [11,33], while the typical thin layer structure signal with the (100) peak at 2θ of 13° ($d = 0.663 \text{ nm}$), attributing to the in-plane structural reflection of bulk C₃N₄ weakens. It clearly reveals the exfoliation of layered C₃N₄ sample. The thickness of C₃N₄-HCl sample can be calculated to be ca. 5.46 nm, corresponding to the above TEM result and further suggesting the successful exfoliation of layered bulk C₃N₄. As for the series of Ni(OH)₂/C₃N₄ samples, some weak broad peaks at around 19° , 33° and 38° , corresponding to (001), (100) and (101) peak of hexagonal $\beta\text{-Ni(OH)}_2$ [26], can be detected, and those intensity is enhanced with the increase of the amount of loading Ni(OH)₂. According to the mode of hexagonal

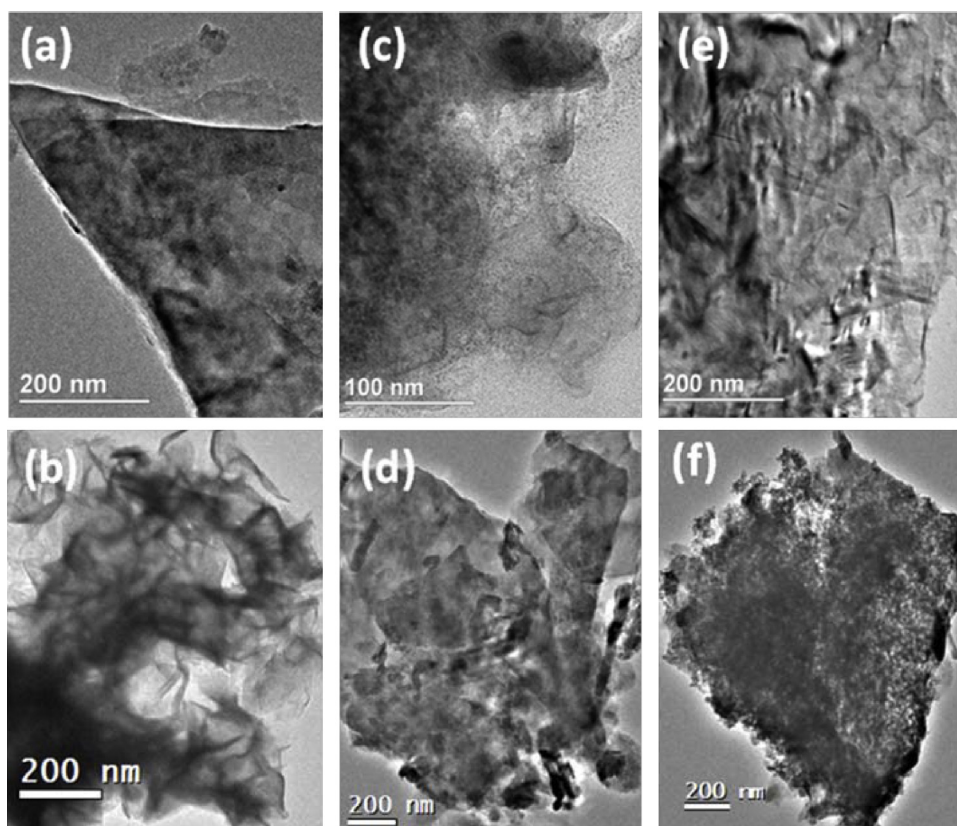


Fig. 2. TEM images of (a) bulk g-C₃N₄; (b) g-C₃N₄ nanosheet; (c) 0.1% Ni(OH)₂/C₃N₄; (d) 0.3% Ni(OH)₂/C₃N₄; (e) 0.5% Ni(OH)₂/C₃N₄; (f) 1% Ni(OH)₂/C₃N₄. The g-C₃N₄ nanosheet sample was synthesized through the process of hydrothermal exfoliation of bulk g-C₃N₄ taking advantage of light concentration of hydrochloric acid as the solvent.

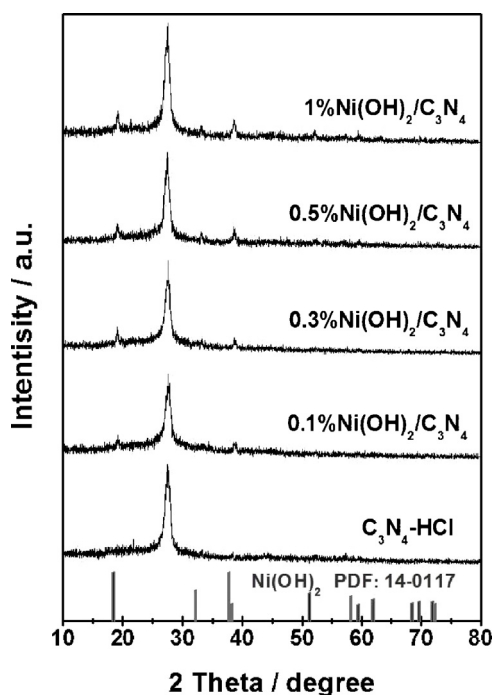


Fig. 3. XRD patterns of studied samples, the standard β -Ni(OH)₂ diffraction peak is also given.

β -Ni(OH)₂, the interplanar space of (001) is about 0.46 nm (Fig. S2). Based on the full-width-at-half-maximum of the (001) peaks in the XRD patterns, the thickness of β -Ni(OH)₂ nanosheets along the c-axis is calculated to be ca. 2.5 nm for the 0.1% Ni(OH)₂/C₃N₄,

about five times of the β -Ni(OH)₂ monolayer. This indicates that the β -Ni(OH)₂ nanosheets formed in this work have been self-assembled to exist as multiple layers. Moreover, the thickness of Ni(OH)₂/C₃N₄ samples is increasing with the increase of Ni(OH)₂ loading (Table S1), which indirectly describes the layer-by-layer formation of Ni(OH)₂ on layered g-C₃N₄. As a comparison, we carried out the hydrothermal synthesis of nickel chloride without bulk g-C₃N₄ adding and found that no solid can be obtained, but when adding urea as the mineralizer, the β -Ni(OH)₂ was formed (Fig. S3). In addition, the bulk g-C₃N₄ will be kept and cannot be exfoliated after the hydrothermal treatment without nickel chloride. These results reveal that the exfoliation of g-C₃N₄ and the formation of β -Ni(OH)₂ nanosheets may simultaneously take place.

The formation of crystallized β -Ni(OH)₂ nanosheets is further confirmed by high-resolution TEM (HRTEM) measurement on the chosen 0.3 wt% Ni(OH)₂/C₃N₄ sample. As shown in Fig. 4a and b (locally enlarged view), the ordered arrangement of lattice fringes suggests the relative high degree of crystallinity of loading Ni(OH)₂. On the other hand, two evident crystal facets with the intersection angle of 60° can be distinguished, as is in good accordance with the intersection between <100> and <010> of hexagonal β -Ni(OH)₂, whose mode is given in Fig. 4c. It is worth being mentioned that free of addition of g-C₃N₄, the irregular hexahedron β -Ni(OH)₂ with size of ca. 30 nm can be observed (Fig. S3), suggesting the necessity of bulk g-C₃N₄ for the formation of ultrathin β -Ni(OH)₂ nanosheets. This is in accordance with above XRD results.

Fourier transform infrared spectra (FTIR) measurement was also carried out with the results given in Fig. 5. As for the bulk g-C₃N₄ sample, some feature peaks located at 813 cm⁻¹, 1000–1760 cm⁻¹ and 2900–3400 cm⁻¹ are clearly observed, which have been attributed to condensed CN heterocycles, stretching and bending modes of the nitrogen containing chemical bond, and

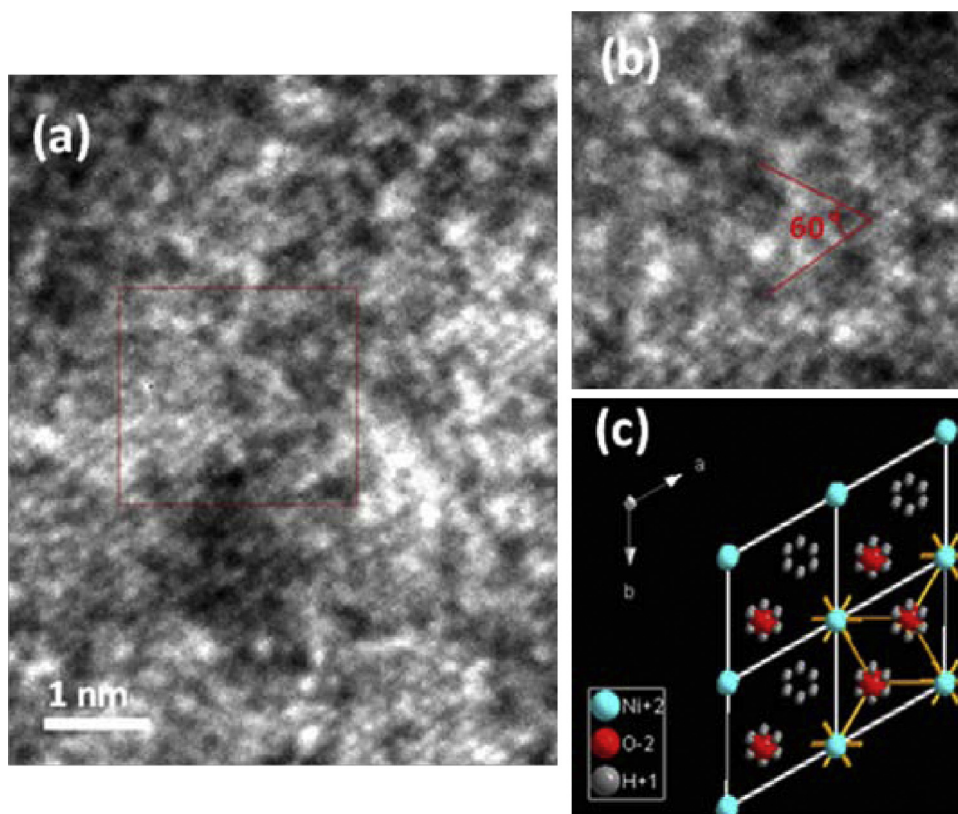


Fig. 4. (a) HRTEM images of 0.3% Ni(OH)₂/C₃N₄ sample; (b) a zoom-in TEM image of red marked region in (a); (c) the mode of (001) crystal face of β-Ni(OH)₂. (For interpretation of the references to colour in this figure legend, the reader is referred to the web version of this article.)

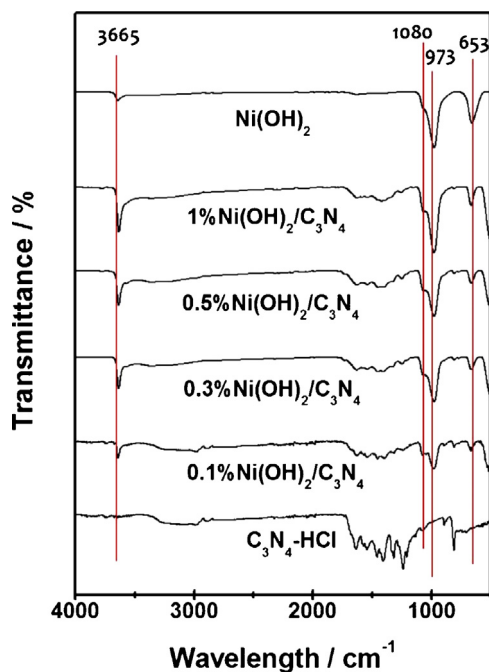


Fig. 5. FTIR spectra of studied samples, the standard β-Ni(OH)₂ diffraction peak is also given.

stretching modes of uncondensed terminal amino groups (–NH₂ or –NH groups) respectively [2,9]. In the case of β-Ni(OH)₂ sample, four infrared peaks at 653, 973, 1080 and 3665 cm^{−1} can be easily identified, which belong to typical signal of β-Ni(OH)₂ [34]. Comparatively, all the feature IR peaks of C₃N₄ and β-Ni(OH)₂ can be

obviously found for the Ni(OH)₂/C₃N₄ hybrids except that most of them are relatively weakened. It means that no obvious destruction of structure occurs. However, it should be pointed out that the intensities of the IR peak at 1080 cm^{−1} assigned to the O–H bend mode [34] are enhanced with the increasing amount of nickel content. This further proves that the formed β-Ni(OH)₂ nanosheets are self-organized layer-by-layer for enhanced thickness in accordance with the TEM and XRD results.

The surface and sub-surface chemical states (in the depth up to 5 nm) of g-C₃N₄ and 0.1%, 0.3% and 1% Ni(OH)₂/C₃N₄ samples are investigated by means of X-ray photoelectron spectroscopy (XPS). As given in Fig. 6a and b, very similar C 1s, N 1s and Ni 2p peaks can be observed for the tested samples. In C 1s region, peaks with binding energies of around 288.4 and 284.9 eV are observed for both g-C₃N₄ and Ni(OH)₂/C₃N₄ samples. The main contribution peak located at 288.4 eV is typically attributed to the sp²-bonded carbon of N=C=N backbone in the aromatic ring of the g-C₃N₄ (see Fig. S1) [11,14]; while the peak at 284.9 eV has been assigned to graphitic carbon [35] or carbon contamination [19–21] or sp²-hybridized of C–N [36,37]. The N1s spectra in Fig. 6(b) can be deconvoluted into three obvious peaks centering at 398, 400.1 and 401 eV. The main peak at 398 eV is a typical signal for sp²-hybridized nitrogen (C=N=C) of triazine rings [35], while the peak centered at 400.1 eV is assigned to N–(C)₃ groups of the skeleton [12,36]. The last weak peak with the binding energy of 401 eV is attributed to the surface uncondensed bridging N atom with C–N–H functional groups attached [36,37]. Noticeably, the relative intensity of the N–(C)₃ groups signal is becoming stronger with the increase of Ni(OH)₂ loading, while that of the uncondensed bridging N groups is decreasing, suggesting the possibility of uncondensed N sites for Ni(OH)₂ nucleation [10]. In the case of Ni 2p region in Fig. 6(c), binding energy values at 874.2 and 856.5 eV, the typical signals of

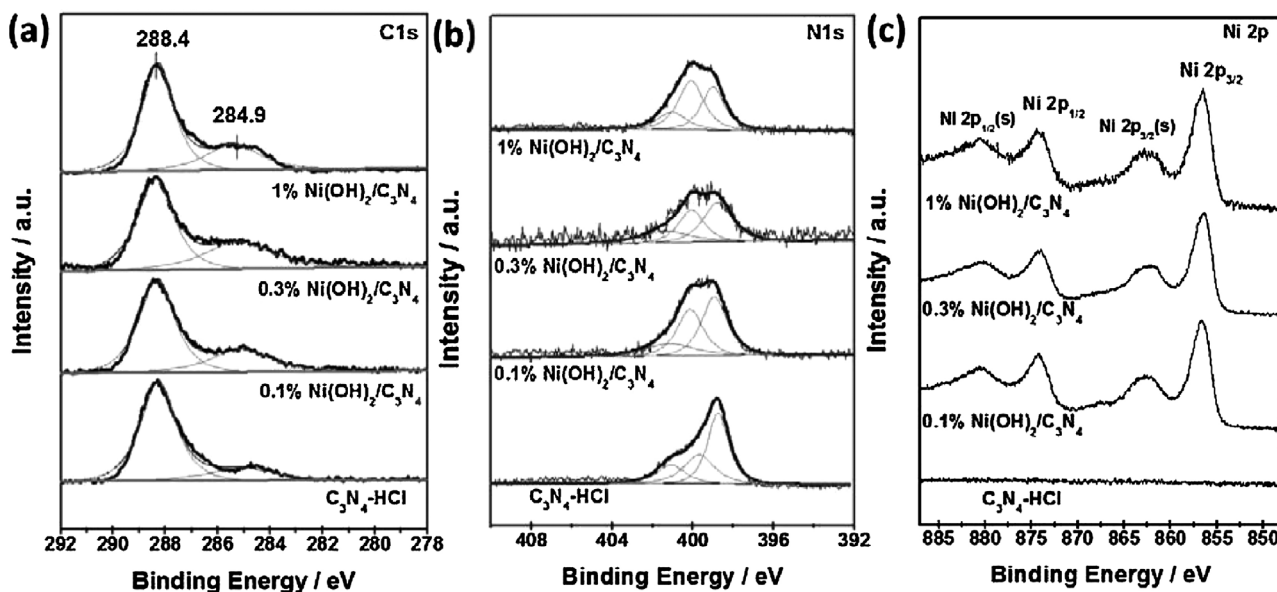


Fig. 6. XPS spectra of g-C₃N₄ and 0.1%, 0.3% and 1% Ni(OH)₂/C₃N₄ samples, (a) C 1s, (b) N 1s and (c) Ni 2p.

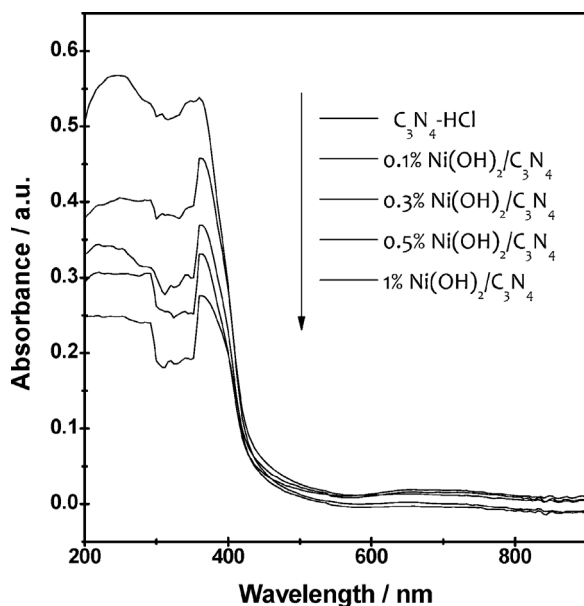


Fig. 7. UV-vis-NIR diffuse reflectance absorption spectra of studied samples.

Ni 2p_{1/2} and Ni 2p_{3/2} are observed in all Ni(OH)₂/C₃N₄ samples but the g-C₃N₄, and a spin-energy separation of 17.7 eV can be detected, indicating the Ni(OH)₂ phase [38]. Also, the Ni 2p spectra of reference β-Ni(OH)₂ is shown in Fig. S5, and slight high binding energy shift of the Ni(OH)₂/C₃N₄ samples can be detected, suggesting the strong interaction between Ni(OH)₂ and g-C₃N₄. The XPS survey spectrums of the studied samples are also given as shown in Fig. S6, clearly suggesting the corresponding elemental composition for the special compounds.

Diffuse reflectance UV-vis-NIR spectroscopy was carried out to study the optical properties of g-C₃N₄ and 0.1%, 0.3%, 0.5% and 1% Ni(OH)₂/C₃N₄ samples. As shown in Fig. 7, all samples show intrinsic absorption in the visible-light region attributed to the band-band transition of g-C₃N₄ support. The absorption edges are almost the same as each other with the threshold value of 430 nm, corresponding to band gap of 2.86 eV for all samples. No obvious red or blue shift of absorption edges can be detected, which may

prove the limitation of Ni(OH)₂ loading, causing unobvious change of electronic structure. However, a decreasing trend in the light absorption can be observed with the increase loading of Ni(OH)₂, resulting from the enhanced scattering of light with the introduction of some amount of foreign Ni(OH)₂ component [39].

3.2. Water splitting performances of β-Ni(OH)₂/g-C₃N₄ nanohybrids

As discussed in the introduction section, Ni(OH)₂ has been widely used and proved to show excellent performance in electrochemical category [27–29]. The g-C₃N₄ layered material is regarded as an efficient visible-light-active photocatalyst with amazing water splitting productivity [2,7,10]. Thinking of above unique aforementioned characteristics of Ni(OH)₂ and g-C₃N₄ materials and with the novel Ni(OH)₂/C₃N₄ lamellar nanohybrids obtained via herein original one-step process in hand, the nanohybrid samples should possess possibly considerable photoelectrical conversion efficiency with the practical application such as water splitting. For special materials objecting to application of water photolysis to hydrogen (H₂) and oxygen (O₂), not only the high-performance generation of photogenerated carriers but also high efficiency of multiple-electron reaction kinetics, involving interface transfer processes and corresponding low water-splitting overpotentials, are required [29,40,41]. To test and verify practical feasibility of our synthesized Ni(OH)₂/C₃N₄ samples, herein, we first applied the g-C₃N₄ and nanohybrids samples to the O₂ evolution reaction (OER) and H₂ evolution reaction (HER) polarization measurements in 0.1 M NaOH solution to obtain the first evidence for the next special water splitting application. The OER characteristics of the studied samples as shown in Fig. 8(a) express a typical positive current caused by electrolysis of water to O₂ in the range of 1.4–1.8 V vs NHE with obvious difference. Typically, g-C₃N₄ nanosheet sample shows the lowermost current density of 0.017 mA cm⁻² with the bias voltage of 1.6 V. When assembling some amount of 2D Ni(OH)₂ nanosheet on g-C₃N₄, a clear identifiable discrepancy can be obtained with the suggestion of the efficient interface transfer efficiency of carriers. Notably, the peak at 1.4 V ascribed to the oxidation of Ni(OH)₂ to NiOOH can be observed, the NiOOH species has been reported to possess the superiority of solving the electrical double layer potential drop

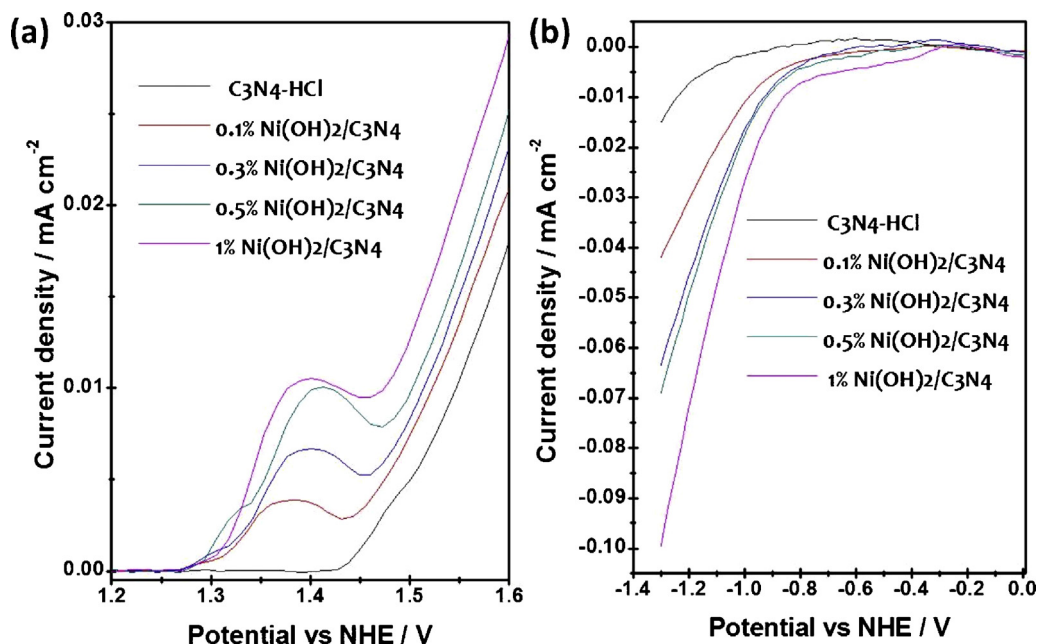


Fig. 8. The OER (a) and HER (b) characteristics of C_3N_4 and $\text{Ni}(\text{OH})_2/\text{C}_3\text{N}_4$ samples. The scan direction with a scan rate of 50 mV s^{-1} for OER is from positive to negative potential and the HER is an opposed direction in 0.1 M NaOH electrolyte solution, Ag/AgCl (saturated KCl) and Pt electrode are used as the reference and counter electrode, respectively.

at the catalyst/electrolyte junction and then be responsible for the low interface barrier of carriers such as photogenerated holes migration [23]. It should be noted that the overpotential slightly moves to lower potential with the increase of $\text{Ni}(\text{OH})_2$ loading. With regard to the HER performances with the scan direction from negative to positive as shown in Fig. 8(b), similar performance trend as the mentioned OER measurements can be easily differentiated with $\text{g-C}_3\text{N}_4$ giving the lowest HER current density. Considering that the above water polarization activity is remarkable, the constructed $\text{Ni}(\text{OH})_2/\text{C}_3\text{N}_4$ nanohybrids should own the considerable water photo-splitting performance.

We employed our synthesized $\text{Ni}(\text{OH})_2/\text{C}_3\text{N}_4$ nanohybrid samples for hydrogen-evolving evolution half reaction of water photo-splitting first and the results are shown in Fig. 9(a). It is seen that both bare $\text{g-C}_3\text{N}_4$ and nanohybrids samples exhibit considerably active rate for hydrogen production from photo-splitting water half reaction. Specifically, $\text{g-C}_3\text{N}_4$ shows the lowest hydrogen generation rate of $49.3 \mu\text{mol h}^{-1}$. However, the reaction rate increases to $75 \mu\text{mol h}^{-1}$ immediately when $0.1\% \text{ Ni}(\text{OH})_2$ is loaded. When the loading amount increases to 0.3% and 0.5% , the hydrogen generation rates are 87.5 and $95.4 \mu\text{mol h}^{-1}$, which are the 1.8 and 1.9 times higher than that of bare $\text{g-C}_3\text{N}_4$, respectively. However, the $1\% \text{ Ni}(\text{OH})_2/\text{C}_3\text{N}_4$ sample does not show the expected increase of reaction rate with a $86.5 \mu\text{mol h}^{-1}$ value, which suggests the optimized loading of $\text{Ni}(\text{OH})_2$ is 0.5% and more $\text{Ni}(\text{OH})_2$ sites act as the photogenerated carriers recombination center [42]. The recycling experiments of hydrogen generation rate were carried out to obtain the stability information of $0.5\% \text{ Ni}(\text{OH})_2/\text{C}_3\text{N}_4$ sample and the result is shown in Fig. 9(b). The hydrogen generation rate keeps unchanged within five cycles in 20 h , revealing the photostabilization of as-synthesized nanohybrid sample. On the other hand, the half reaction of hydrogen evolution from water splitting can be affected by the hole scavengers [9], and we also chose other two conventional scavengers, methanol and ethanol for comparison (Table S2). The similar reaction activity with previous report can be found with triethanolamine exhibiting the highest HER rate [9].

Based on negative shift of overpotential of OER characteristics in Fig. 8, the other half-reaction of oxygen generation rate from water photo-splitting was also carried out as given in Fig. 10. Obviously, these results present a similar trend as hydrogen conditions in Fig. 9(a) with $0.5\% \text{ Ni}(\text{OH})_2/\text{C}_3\text{N}_4$ sample exhibiting the best performance. Specifically, $\text{g-C}_3\text{N}_4$ sample shows the $7.4 \mu\text{mol h}^{-1}$ apparent reaction rate, which is close to the previous literature report [13]. Also, the $0.5\% \text{ Ni}(\text{OH})_2/\text{C}_3\text{N}_4$ reference sample synthesized through impregnation method was carried out on water photosplitting and the results are given in Fig. S8. Clearly, hydrogen and oxygen generation rates show the similar level of the water splitting ability as bare $\text{g-C}_3\text{N}_4$, which illustrates the superiority and importance of layered $\text{Ni}(\text{OH})_2/\text{C}_3\text{N}_4$ structure. The photocatalytic H_2 generation of synthesized $\beta\text{-Ni}(\text{OH})_2/\text{C}_3\text{N}_4$ samples was also compared with the reported values of literatures as shown in Table S3, which clearly suggested the excellent photogenerated carriers separation performance of our studied samples.

Furthermore, to further underline the importance of $\text{Ni}(\text{OH})_2/\text{C}_3\text{N}_4$ layered nanohybrid structure for the separation of photogenerated carriers, we also took advantage of photoelectrical detecting technique *i.e.* photocurrent response ability. As displayed in Fig. 10(b), all samples show almost flat photocurrent signal under no illumination condition and oppositely, obvious values appeared once adding simulated sunlight, suggesting the nature of studied semiconductors. The bare $\text{g-C}_3\text{N}_4$ gives the lowest photocurrent value and then increases along with $\text{Ni}(\text{OH})_2$ loading. It can be observed that the photocurrent performance is gradually improved until the maximum by $1\% \text{ Ni}(\text{OH})_2/\text{C}_3\text{N}_4$, which is not similar to the water splitting situation, where the 0.5% sample shows the best (Figs. 9 (a) and 10 (a)). Noting that the bias voltage is needed for the photocurrent measurement, it ensures the directional movement of photogenerated carriers from irradiant studied samples. Also, the above photocurrent results indirectly reflect the fact of the most photogenerated free carriers from the $1\% \text{ Ni}(\text{OH})_2/\text{C}_3\text{N}_4$ sample. In the case of powder system, as discussed above, the more foreign components are introduced, the more recombination sites will be formed and then the lower the photolysis efficiency of water [42]. On the other

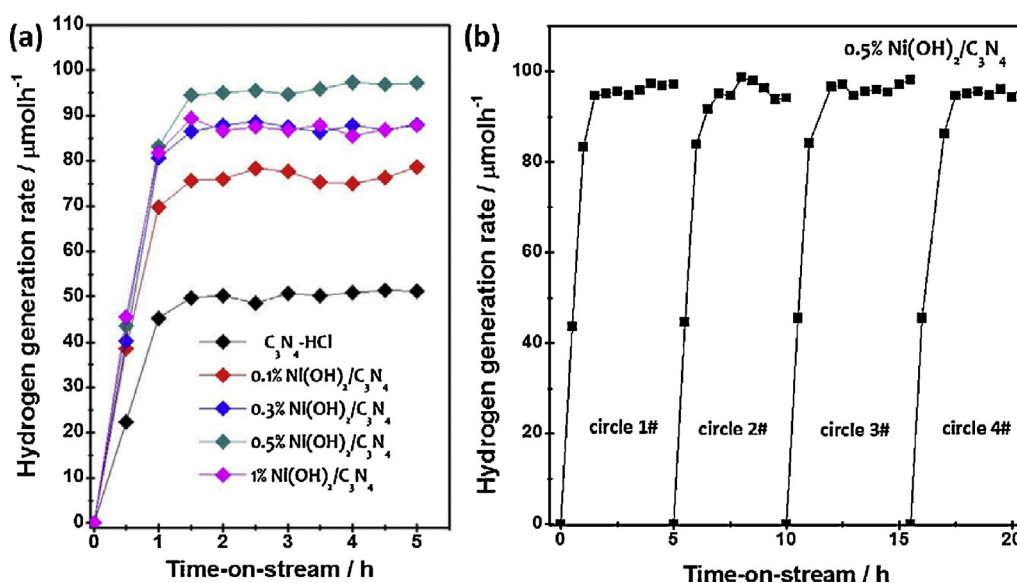


Fig. 9. (a) Hydrogen generation rate from water photo-splitting under layered g-C₃N₄ and series of Ni(OH)₂/C₃N₄ samples; (b) the cycled hydrogen evolution performance under the 0.5% Ni(OH)₂/C₃N₄ sample. Reaction conditions: 0.1 g catalyst, 200 mL 10% (v/v) triethanolamine-water solution, 1% Pt was *in situ* loaded as the co-catalyst, 150 W xenon lamp without filters used as the light source. Note: the conversational relationship between GC signal and the amount of gas evolution can be found in Fig. S7.

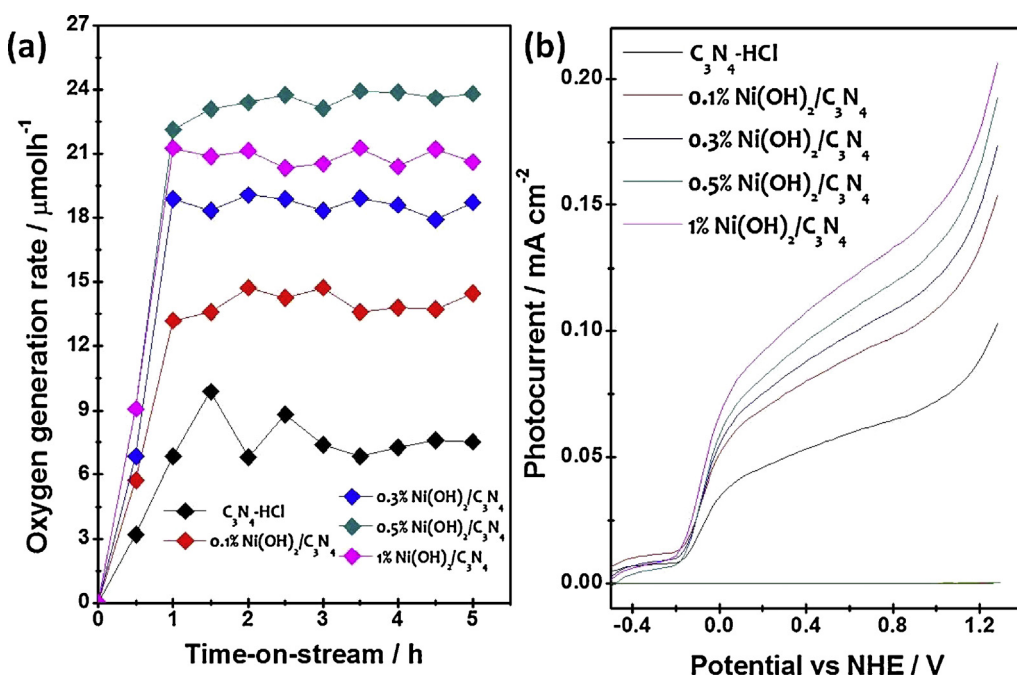


Fig. 10. (a) Oxygen generation rate from water photo-splitting under layered g-C₃N₄ and series of Ni(OH)₂/C₃N₄ samples; Reaction conditions: 0.1 g catalyst, 200 mL 0.01 M AgNO₃ solution, 150 W xenon lamp without filters used as the light source; (b) Photocurrent response based on studied samples in 0.5 M Na₂SO₄ solution.

hand, the nature of photocurrent response is photo-electrical water oxidation on given catalysts. The here results presented in Fig. 10(b) also suggest that the β-Ni(OH)₂ layer act as the receiving sites of photogenerated holes and then facilitate the water oxidation [43]. Photoluminescence (PL) spectroscopy was conducted here to further suggest the photogenerated carriers' separation efficiency for the direct interpretation of the carrier receiving sites of loading Ni(OH)₂ [13,39]. Satisfactorily, as shown in Fig. S9, the photoluminescence of Ni(OH)₂/C₃N₄ samples is quenched compared to bare g-C₃N₄ and the result exhibits similar trend with above water photosplitting ability, which indirectly confirms the previous assumption, that is, Ni(OH)₂ layers attract the holes and then improve the water oxidation; and correspondingly, the

lifetime of photogenerated electrons is lengthened as a results of enhanced hydrogen generation rate.

3.3. Direct water splitting performances based on β-Ni(OH)₂/g-C₃N₄ nanohybrids

As has been discussed that the direct photocatalytic water splitting into H₂ and O₂ is limited by the photogenerated holes oxidizing water step [15]. And the fundamental reasons are the limited life time of holes and the catalyst/electrolyte junction interface barrier of the carriers' migration [23]. Based on the above experiment results of electrolytic water performance, photocatalytic H₂ and O₂ generation, the photogenerated carriers' life times have been

Table 1
The direct water splitting performance based on g-C₃N₄ series photocatalysts.

Entry	Photocatalyst	Illumination	Intensity/mW/cm ²	Gas generation rate/ $\mu\text{mol h}^{-1}$		AQY/%
				H ₂	O ₂	
1	g-C ₃ N ₄	Xenon lamp	–	–	–	–
2	0.1% Ni(OH) ₂ /g-C ₃ N ₄	Xenon lamp	–	1.2	0.5	–
3	0.3% Ni(OH) ₂ /g-C ₃ N ₄	Xenon lamp	–	2.8	1.5	–
4	0.5% Ni(OH) ₂ /g-C ₃ N ₄	Xenon lamp	–	3.9	2.1	–
5	1% Ni(OH) ₂ /g-C ₃ N ₄	Xenon lamp	–	2.2	1.2	–
6	0.5% Ni(OH) ₂ /g-C ₃ N ₄ -Pt	Xenon lamp	–	15.5	7.8	–
7	0.5% Ni(OH) ₂ /g-C ₃ N ₄	365 nm LED	8.3	4.2	2.2	0.46
8	0.5% Ni(OH) ₂ /g-C ₃ N ₄	405 nm LED	8.6	3.6	1.7	0.37
9	0.5% Ni(OH) ₂ /g-C ₃ N ₄	425 nm LED	5.4	3.1	1.5	0.32
10	0.5% Ni(OH) ₂ /g-C ₃ N ₄	460 nm LED	6.3	–	–	–
11	0.5% Ni(OH) ₂ /g-C ₃ N ₄ -Pt	405 nm LED	8.6	14.2	7.2	1.48

prolonged artificially and successfully, especially the holes for β -Ni(OH)₂/g-C₃N₄ nanohybrids compared to bare g-C₃N₄. Then we applied our nanohybrid samples to the direct water splitting reaction under the 150 W xenon lamp and different LED illumination. The corresponding photocatalytic results are shown in Table 1. Bare g-C₃N₄ presents the limited gas evolution beyond the GC detection limit (entry 1), although it shows the given mass of hydrogen or oxygen generation under the certain sacrificial reagents (Figs. 9 and 10). When loading some amount of β -Ni(OH)₂ on the g-C₃N₄ surface to construct the layered heterojunction structure, the H₂ and O₂ evolution steadily in a stoichiometric ratio of 2:1 was detected with the 0.5% β -Ni(OH)₂ showing the best (entries 2–5). The lifetime of photogenerated holes can be indirectly prolonged through accelerating the reaction of photogenerated electrons. To improve the direct overall water splitting performance, 1% Pt was *in situ* loaded on the g-C₃N₄ surface through receiving the photogenerated electrons based on the 0.5% Ni(OH)₂/g-C₃N₄ photocatalyst. As shown in Fig. S10, Pt species were indeed found on the g-C₃N₄ surface. The water splitting performance of 0.5% Ni(OH)₂/g-C₃N₄-Pt photocatalyst was listed in entry 6, the simultaneous evolution of H₂ and O₂ gases showed ca. 4 times higher than 0.5% Ni(OH)₂/g-C₃N₄. We also tested the performance under the different LEDs monochromatic light irradiation based on the 0.5% Ni(OH)₂/g-C₃N₄ sample (entries 7–10). As expected, the overall water splitting activity was decreasing with increasing the LED wavelength with the UV (365 nm in entry 7) condition best. Furthermore, the visible light condition (405 nm in entry 11) based on 0.5% Ni(OH)₂/g-C₃N₄-Pt sample was also carried out with the 14.2 and 7.2 $\mu\text{mol h}^{-1}$ for H₂ and O₂ evolution. Also, the apparent quantum yield (AQY) under this condition for the overall water splitting reaction was calculated to be 1.48%. This is lower than the value of 4.01% of our previous report [31]. However, it is a negligible value that the direct pure water splitting can proceed based on the g-C₃N₄ semiconductor. Also, the 4-electron water splitting process can be achieved successfully and steadily through the inorganic β -Ni(OH)₂ prolonging the lifetime of photogenerated holes [43].

4. Conclusions

In conclusion, Ni(OH)₂/C₃N₄ lamellar nanohybrids are prepared by the one-pot hydrothermal method. The bulk layered g-C₃N₄ is thinned through here *in situ* exfoliated method with the simultaneous nucleation of Ni(OH)₂ nanosheet. The bulk g-C₃N₄ layered structure provides assistance for the inserting of nickel ions and then for heterogeneous growth with exposed (001) facets. Meanwhile, the formed Ni(OH)₂ nanosheets promote the dissociation of g-C₃N₄ supporter. Characterization results from TEM, HRTEM and XRD clearly suggest the obtained Ni(OH)₂/C₃N₄ compounds are layer-by-layer structure with the ca. 5 nm thickness of Ni(OH)₂; further results from FTIR and XPS spectrums provide information

on the weak interaction between Ni(OH)₂ and g-C₃N₄ supporter. It is established that the absorption range of the synthesized samples does not show red or blue shift according to the following UV–vis–NIR diffuse reflectance absorption spectra.

The obtained layered Ni(OH)₂/C₃N₄ samples show excellent electrochemical OER and HER performance with corresponding negative and positive shift relative to bare g-C₃N₄, and then accelerating the interface transfer processes of photogenerated carriers owing to the low water-splitting overpotentials. 0.5% Ni(OH)₂ loading is proved to be the optimized content for H₂ and O₂ generation rate. The photocurrent results with show the response value increases along with the increase of Ni(OH)₂ loading, which suggests the layered Ni(OH)₂ acts as the receiving sites of photogenerated holes. The quenched PL results of Ni(OH)₂/C₃N₄ samples compared to bare g-C₃N₄ suggest the inhibiting effect on photogenerated carriers, and therefore, enhance the water photolysis to hydrogen and oxygen rates. The direct water splitting was also carried out with the highest AQY of 1.48% under 405 nm visible light irradiation when the Ni(OH)₂/C₃N₄ sample loading some amount of Pt H₂-evolution co-catalyst. The layer-by-layer Ni(OH)₂/C₃N₄ nanohybrids with excellent performance of water photosplitting, which no doubt help us understand the advantage of 2D materials for free carriers separation; also, the suggested *in situ* exfoliation and formation layered nanohybrid compounds can provide a new strategy for designing new 2D nanohybrids and promoting solar energy conversion.

Acknowledgements

We thank Prof. Fuxiang Zhang at Dalian Institute of Chemical Physics for insightful discussion. We thank the support from the National University Research Fund (GK261001009); the Changjiang Scholar and Innovative Research Team (IRT_14R33), the 111 Project (B14041), the Fundamental Research Funds for the Central Universities (GK201602007) and the Chinese National 1000-Talent-Plan program are also acknowledged.

Appendix A. Supplementary data

Supplementary data associated with this article can be found, in the online version, at <http://dx.doi.org/10.1016/j.apcatb.2016.04.048>.

References

- [1] Y. Sun, S. Gao, Y. Xie, Chem. Soc. Rev. 43 (2014) 530–546.
- [2] M. Zhang, X. Wang, Energy Environ. Sci. 7 (2014) 1902–1906.
- [3] J. Yan, T. Wang, G. Wu, W. Dai, N. Guan, L. Li, J. Gong, Adv. Mater. 27 (2015) 1580–1586.
- [4] M.M.Y.A. Alsaif, K. Latham, M.R. Field, D.D. Yao, N.V. Medehkar, G.A. Beane, R.B. Kaner, S.P. Russo, J. Zhen Ou, K. Kalantar-zadeh, Adv. Mater. 26 (2014) 3931–3937.

- [5] S. Yang, Y. Gong, J. Zhang, L. Zhan, L. Ma, Z. Fang, R. Vajtai, X. Wang, P.M. Ajayan, *Adv. Mater.* 25 (2013) 2452–2456.
- [6] J. Zhang, Y. Chen, X. Wang, *Energy Environ. Sci.* 2015 (8) (2015) 3092–3108.
- [7] C. Huang, C. Chen, M. Zhang, L. Lin, X. Ye, S. Lin, M. Antonietti, X. Wang, *Nat. Commun.* 6 (2015) 7698.
- [8] J. Liu, S. Wen, Y. Hou, F. Zuo, G.J.O. Beran, P. Feng, *Angew. Chem. Int. Ed.* 52 (2013) 3241–3245.
- [9] X. Wang, K. Maeda, A. Thomas, K. Takanabe, G. Xin, J.M. Carlsson, K. Domen, M. Antonietti, *Nat. Mater.* 8 (2009) 76–80.
- [10] S. Cao, J. Low, J. Yu, M. Jaroniec, *Adv. Mater.* 27 (2015) 2150–2176.
- [11] J. Xu, L. Zhang, R. Shi, Y. Zhu, *J. Mater. Chem. A* 1 (2013) 14766–14772.
- [12] J. Zhang, M. Grzelczak, Y. Hou, K. Maeda, K. Domen, X. Fu, M. Antonietti, X. Wang, *Chem. Sci.* 3 (2012) 443–446.
- [13] G. Zhang, S. Zang, X. Wang, *ACS Catal.* 5 (2015) 941–947.
- [14] Y. Hou, A.B. Laursen, J. Zhang, G. Zhang, Y. Zhu, X. Wang, S. Dahl, I. Chorkendorff, *Angew. Chem. Int. Ed.* 52 (2013) 3621–3625.
- [15] J.B. Sambur, T.-Y. Chen, E. Choudhary, G. Chen, E.J. Nissen, E.M. Thomas, N. Zou, P. Chen, *Nature* 530 (2016) 77–80.
- [16] Y. Zheng, L. Lin, B. Wang, X. Wang, *Angew. Chem. Int. Ed.* 54 (2015) 12868–12884.
- [17] G. Zhang, M. Zhang, X. Ye, X. Qiu, S. Lin, X. Wang, *Adv. Mater.* 26 (2014) 805–809.
- [18] G. Zhang, S. Zang, Z.-A. Lan, C. Huang, G. Li, X. Wang, *J. Mater. Chem. A* 3 (2015) 17946–17950.
- [19] G. Zhang, C. Huang, X. Wang, *Small* 11 (2015) 1215–1221.
- [20] G. Zhang, G. Li, X. Wang, *ChemCatChem* 7 (2015) 2864–2870.
- [21] D. Zheng, G. Zhang, X. Wang, *Appl. Catal. B* 179 (2015) 479–488.
- [22] K. Wang, Q. Li, B. Liu, B. Cheng, W. Ho, J. Yu, *Appl. Catal. B* 176–177 (2015) 44–52.
- [23] T.W. Kim, K.-S. Choi, *Science* 343 (2014) 990–994.
- [24] J. Yang, D. Wang, H. Han, C. Li, *Acc. Chem. Res.* 46 (2013) 1900–1909.
- [25] J. Luo, J.-H. Im, M.T. Mayer, M. Schreier, M.K. Nazeeruddin, N.-G. Park, S.D. Tilley, H.J. Fan, M. Grätzel, *Science* 345 (2014) 1593–1596.
- [26] R. Subbaraman, D. Tripkovic, K.-C. Chang, D. Strmcnik, A.P. Paulikas, P. Hirunsit, M. Chan, J. Greeley, V. Stamenkovic, N.M. Markovic, *Nat. Mater.* 11 (2012) 550–557.
- [27] M. Gao, W. Sheng, Z. Zhuang, Q. Fang, S. Gu, J. Jiang, Y. Yan, *J. Am. Chem. Soc.* 136 (2014) 7077–7084.
- [28] N. Danilovic, R. Subbaraman, D. Strmcnik, K.-C. Chang, A.P. Paulikas, V.R. Stamenkovic, N.M. Markovic, *Angew. Chem.* 124 (2012) 12663–12666.
- [29] X. Xia, J. Luo, Z. Zeng, C. Guan, Y. Zhang, J. Tu, H. Zhang, H.J. Fan, *Sci. Rep.* 2 (2012) 981.
- [30] F. Lin, S.W. Boettcher, *Nat. Mater.* 13 (2014) 81–86.
- [31] J. Yan, H. Wu, H. Chen, Y. Zhang, F. Zhang, S. Liu, *Appl. Catal. B* 191 (2016) 130–137.
- [32] J. Xie, X. Sun, N. Zhang, K. Xu, M. Zhou, Y. Xie, *Nano Energy* 2 (2013) 65–74.
- [33] Y. Cui, J. Zhang, G. Zhang, J. Huang, P. Liu, M. Antonietti, X. Wang, *J. Mater. Chem.* 21 (2011) 13032–13039.
- [34] D.S. Hall, D.J. Lockwood, S. Poirier, C. Bock, B.R. MacDougall, *J. Phys. Chem. A* 116 (2012) 6771–6784.
- [35] D.J. Martin, K. Qiu, S.A. Shevlin, A.D. Handoko, X. Chen, Z. Guo, J. Tang, *Angew. Chem. Int. Ed.* 53 (2014) 1–7.
- [36] S.M. Lyth, Y. Nabae, S. Moriya, S. Kuroki, M. Kakimoto, J. Ozaki, S. Miyata, *J. Phys. Chem. C* 113 (2009) 20148–20151.
- [37] X. She, H. Xu, Y. Xu, J. Yan, J. Xia, L. Xu, Y. Song, Y. Jiang, Q. Zhang, H. Li, *J. Mater. Chem. A* 2 (2014) 2563–2570.
- [38] F.Q. Zhang, D. Zhu, X. Chen, X. Xu, Z. Yang, C. Zou, K.Q. Yang, S.M. Huang, *Phys. Chem. Chem. Phys.* 16 (2014) 4186–4192.
- [39] J. Yan, G. Wu, N. Guan, L. Li, Z. Li, X. Cao, *Phys. Chem. Chem. Phys.* 15 (2013) 10978–10988.
- [40] K. Maeda, *Chem. Commun.* 49 (2013) 8404–8406.
- [41] K. Maeda, *ACS Catal.* 4 (2014) 1632–1636.
- [42] J. Yan, G. Wu, N. Guan, L. Li, *Appl. Catal. B* 152–153 (2014) 280–288.
- [43] Z. Wang, G. Liu, C. Ding, Z. Chen, F. Zhang, J. Shi, C. Li, *J. Phys. Chem. C* 119 (2015) 19607–19612.